



Constructing surface micro-electric fields on hollow single-atom cobalt catalyst for ultrafast and anti-interference advanced oxidation

Changqing Zhu^a, Yu Nie^a, Shafei Zhao^b, Zhongwei Fan^a, Fuqiang Liu^{a,*}, Aimin Li^a

^a State Key Laboratory of Pollution Control and Resource Reuse, School of the Environment, Nanjing University, Nanjing 210023, PR China

^b School of Chemistry and Chemical Engineering, Nanjing University, Nanjing 210023, PR China

ARTICLE INFO

Keywords:

Single-atom cobalt catalyst
Advanced oxidation process
Pollution control
Peroxymonosulfate
Micro-electric field

ABSTRACT

Reactive oxygen species (ROSs) quenching by inorganic anions and natural organic matter (NOM) restricts efficiency upgradation of advanced oxidation process. Here a novel '4H' carbon polyhedral catalyst featuring hollow structure, high-density single-atom cobalt sites, high adsorbability and high conductivity is designed to activate peroxymonosulfate (PMS) for bisphenol A (BPA) degradation. 91.62% of BPA is removed within 15 s, and the catalyst-dose-normalized kinetic rate constant reaches $92.92 \text{ L min}^{-1} \text{ g}^{-1}$, outdistancing reported values. Meanwhile, the composite demonstrates excellent anti-interference ability against anions and NOM. Moreover, the catalyst-loaded column reactor realizes BPA zero discharge for impressive 12.19 days. Experimental and theoretical evidences reveal that PMS bound on the single-atom cobalt site excites radial micro-electric field on the carbon support to drive electron extraction from co-adsorbed BPA, which fundamentally eliminates ROSs quenching and guarantees robust pollutant oxidation. This work can guide the '4H' catalyst design and refresh the atomic-level understanding of electron-transfer pathway.

1. Introduction

The ever-growing production and use of organic chemicals have remarkably promoted social progress, but their uncontrolled discharge into waters causes serious harm to the ecological environment [1]. Among the technologies for wastewater treatment, the advanced oxidation process (AOP) is powerful in degrading refractory organics through the generation of reactive oxygen species (ROSs, e.g. hydroxyl radical ($\bullet\text{OH}$), sulfate radical ($\text{SO}_4^{\bullet-}$), superoxide radical ($\text{O}_2^{\bullet-}$)) [2]. Recently, the peroxymonosulfate-based AOP (PMS-AOP) has attracted considerable attention due to the excellent oxidizing ability and wide work pH range [3]. Various catalysts with precisely designed structures have been developed for PMS activation to yield ROSs [4,5]. However, due to the high reactivity and low selectivity, the produced ROSs are inevitably consumed by the inorganic anions and natural organic matter (NOM) co-existing with targeted pollutants, resulting in the sluggish kinetics [6,7]. It's thus imperative to exploit catalysts with both high efficiency and anti-interference performance for the practical application.

In the heterogeneous PMS-AOP, the pollutant adsorption onto catalysts has been identified as a critical step for the efficient catalytic

oxidation [8]. Based on it, constructing the dual-site materials, with both adsorptive and catalytic sites to selectively enrich targeted contaminants and confine the degradation reaction within the catalyst, could reduce the disturbance from substances left in bulk solution. Meanwhile, studies demonstrated that the complexes of PMS and conductive carbon catalysts realized pollutant decomposition through a catalyst-mediated electron-transfer mechanism without producing ROSs [9,10]. This process followed a two-step route: PMS was captured by the catalyst to form a surface complex; next, the catalyst-PMS complex abstracted electrons from adsorbed pollutants to initiate the oxidation [9]. Such strategy avoided the ROSs consumption but was restricted by the low intrinsic activity of carbons for PMS activation. More importantly, the directional electron transport from contaminants to PMS on the catalyst implied the existence of a surface electric field. However, the origin, distribution and profile of this electric field all remained unclear, which hindered the further development of PMS-AOP.

Recently, the single-atom catalysts (SACs) with atomically dispersed metal centers have exhibited distinguished catalytic activity in various reactions due to the unique electronic structure and maximized atom utilization [11–14]. Among the supports for SACs, the hollow nitrogen-doped graphitic carbon featuring an inner void was ideal,

* Correspondence to: State Key Laboratory of Pollution Control and Resource Reuse National Engineering Research Center for Organic Pollution Control and Resource Reuse School of the Environment, Nanjing University No. 163 Xianlin Avenue, Nanjing 210023, P.R.China.

E-mail address: lfq@nju.edu.cn (F. Liu).

<https://doi.org/10.1016/j.apcatb.2021.121057>

Received 14 October 2021; Received in revised form 10 December 2021; Accepted 29 December 2021

Available online 31 December 2021

0926-3373/© 2021 Elsevier B.V. All rights reserved.

which could effectively adsorb organic pollutants, conduct electrons, and maximize the material usage by preserving the reactive surface while eliminating the inactive bulk interior [15,16]. Meanwhile, the isolated metal-N-C sites with unsaturated coordination structure favored the complexation with PMS [17–20]. Hence, new opportunities could be offered by the hollow carbon-supported SACs to accomplish highly efficient pollutant degradation in complex water matrices via the above electron-transfer mechanism. Moreover, the SACs with uniform active sites provided an atomic-scale perspective to understand the structure-activity relationship [21], which might shed new light on the PMS-AOP chemistry.

Herein, a pyrolysis-pickling strategy was applied to convert core-shell zeolitic imidazolate frameworks into graphitized carbon polyhedrons featuring the hollow structure, high-density single-atom cobalt sites, high adsorbability and high conductivity. The as-synthesized composite exhibited superior catalytic activity and excellent tolerance to inorganic anions and NOM in bisphenol A (BPA) degradation via PMS activation. BPA was a frequently detected chemical in water systems with the concentration level ranging from ng L^{-1} to $\mu\text{g L}^{-1}$, which could induce endocrine disorders and disrupt the hormonal balance of animals and humans [22]. The ROSs quenching experiments and electron spin resonance detection confirmed that the oxidative decomposition of BPA was governed by the desired electron-transfer process rather than the ROSs pathway. Based on electrochemical analyses and theoretical calculations, the ultrafast and anti-interference performance was attributed to the in-situ construction of abundant radial micro-electric fields by PMS and single-atom Co sites, and the formation mechanism of the electric field was firstly uncovered at the atomic level. Moreover, the catalyst was loaded onto a self-built column reactor to evaluate its practical applicability in continuously treating large amounts of polluted waters. Overall, this work will guide the '4H' catalyst design and advance the atomic-level knowledge of PMS-AOP for water remediation.

2. Materials and methods

2.1. Chemicals and materials

The humic acid (HA) was purchased from Sigma-Aldrich (Shanghai, China). The bisphenol A (BPA), methanol, oxone ($2\text{KHSO}_5\cdot\text{KHSO}_4\cdot\text{K}_2\text{SO}_4$, as the source of PMS), zinc nitrate hexahydrate ($\text{Zn}(\text{NO}_3)_2\cdot 6\text{H}_2\text{O}$), 2-methylimidazole (2-MIM), ammonium chloride (NH_4Cl), sulfuric acid (H_2SO_4), sodium hydroxide (NaOH), cobalt nitrate hexahydrate ($\text{Co}(\text{NO}_3)_2\cdot 6\text{H}_2\text{O}$), sodium sulfate (Na_2SO_4), sodium chloride (NaCl), sodium bicarbonate (NaHCO_3), sodium dihydrogen phosphate (NaH_2PO_4), sodium nitrate (NaNO_3), ethanol, *L*-histidine, potassium thiocyanate (KSCN), *tert*-butyl alcohol, nitro blue tetrazolium chloride monohydrate (NBT), *p*-benzoquinone, methyl orange, phenol and sulfamethoxazole were bought from Sinopharm Chemical Reagent Co., Ltd. (China). All chemicals used were analytically pure. Ultrapure water from the Milli-Q Plus system (Millipore, Bedford, USA) was used for washing and preparing stock solutions.

2.2. Material preparation

2.2.1. Synthesis of ZIF-8 and ZIF-67

Firstly, the 2-MIM (30.80 g, 0.375 mol) and $\text{Zn}(\text{NO}_3)_2\cdot 6\text{H}_2\text{O}$ (29.75 g, 0.10 mol) were fully dissolved into the methanol (750 mL), respectively [23]. Then the 2-MIM solution was added to $\text{Zn}(\text{NO}_3)_2\cdot 6\text{H}_2\text{O}$ solution. After the mixed solution was agitated at 25°C for 24 h, the obtained precipitates (ZIF-8) were centrifuged, washed and dried for further use. To prepare ZIF-67, $\text{Co}(\text{NO}_3)_2\cdot 6\text{H}_2\text{O}$ (29.10 g, 0.10 mol) was used instead of $\text{Zn}(\text{NO}_3)_2\cdot 6\text{H}_2\text{O}$ without changing other procedures.

2.2.2. Synthesis of Core-Shell ZIF-8@67 and ZIF-67@8

To synthesize core-shell ZIF-8@67, the ZIF-8 (2.5 g) was firstly dispersed in methanol (500 mL) under ultrasound [23]. Meanwhile, $\text{Co}(\text{NO}_3)_2\cdot 6\text{H}_2\text{O}$ (29.10 g, 0.10 mol) and 2-MIM (30.80 g, 0.375 mol) were severally dissolved in methanol (500 mL). Afterwards, the $\text{Co}(\text{NO}_3)_2\cdot 6\text{H}_2\text{O}$ solution was added to the dispersion solution of ZIF-8, then the 2-MIM solution was introduced into the mixture. After continuous agitation at 25°C for 24 h, the precipitates were centrifuged, washed then dried. Moreover, ZIF-8@67 samples with different ZIF-67 loading amounts were fabricated by changing the $\text{Co}(\text{NO}_3)_2\cdot 6\text{H}_2\text{O}$ dosages to 0.05, 0.15 and 0.20 mol, respectively, with keeping the same molar ratio of $\text{Co}(\text{NO}_3)_2\cdot 6\text{H}_2\text{O}$ to 2-MIM. The ZIF-67@8 was prepared by adding $\text{Zn}(\text{NO}_3)_2\cdot 6\text{H}_2\text{O}$ (29.75 g, 0.10 mol) and 2-MIM (30.80 g, 0.375 mol) solutions into the dispersion solution of ZIF-67 with no changes of other procedures.

2.2.3. Synthesis of ZIF-8-C, ZIF-67-C, ZIF-8@67-C and ZIF-67@8-C

The ZIF-8, ZIF-67, ZIF-8@67 and ZIF-67@8 samples were placed into the tube furnace where the temperature was increased at 2°C min^{-1} to 950°C and maintained for 2 h in Ar. The obtained powders were stirred in $1.0\text{ mol L}^{-1}\text{H}_2\text{SO}_4$ at 80°C for 4 h to eliminate accessible Co species, followed by being washed till $\text{pH} \approx 7.0$ and dried to yield ZIF-8-C, ZIF-67-C, ZIF-8@67-C and ZIF-67@8-C, respectively. Specially, to investigate the effect of pyrolysis temperatures on the catalytic performance of ZIF-8@67-C, 850 and 750°C were also used to pyrolyze ZIF-8@67 precursor. To study the impact of ZIF-67 loading amounts on the catalysis, ZIF-8@67 samples with different ZIF-67 contents were also calcined under 950°C .

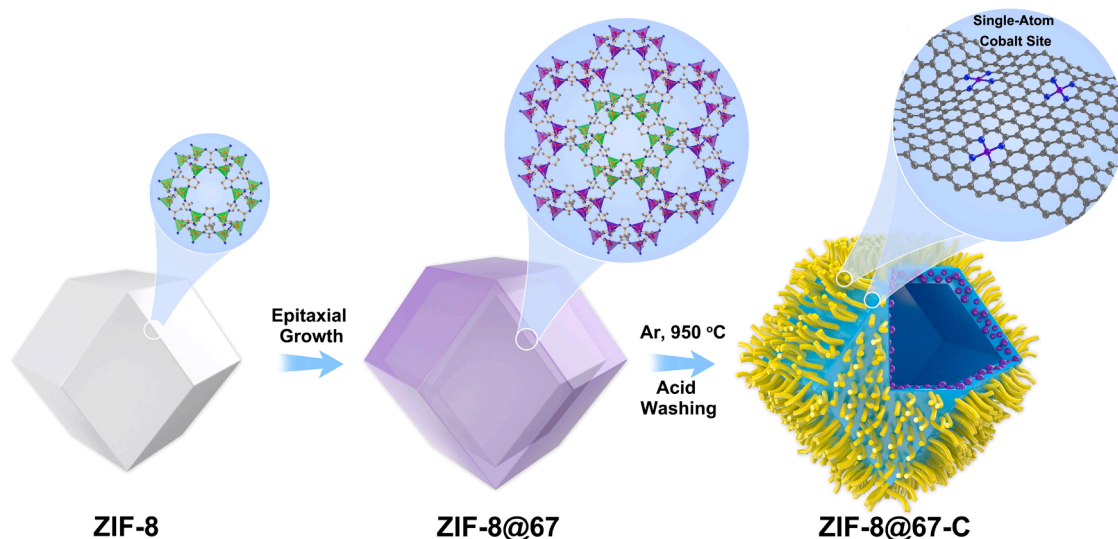
The details including material characterizations, catalytic degradation procedure, analytic methods and computational methods were presented in the Texts S1–4.

3. Results and discussion

3.1. Synthesis and characterization

The synthesis procedure of the hollow graphitized carbon polyhedron (named as ZIF-8@67-C) was illustrated in Scheme 1. Firstly, the ZIF-8@67 precursor with core-shell structure was prepared through the epitaxial growth of ZIF-67 on ZIF-8 surface (Figs. S1–3) [23]. Afterwards, the precursor was pyrolyzed at 950°C in Ar and underwent acid washing to eliminate unstable Co species to obtain the ZIF-8@67-C (Fig. S4).

The scanning and transmission electron microscopy (SEM and TEM) micrographs in Figs. 1a–c revealed that ZIF-8@67-C presented a hollow polyhedron morphology with a well-defined cavity surrounded by the carbon shell. Meanwhile, numerous carbon nanotubes (CNTs) and Co nanoparticles (NPs) of 20–30 nm were anchored on the surface and embedded in the shell, respectively. The high-resolution TEM (HRTEM) image in Fig. 1d showed the fringe spacings of 0.205 and 0.338 nm belonging to the (111) plane of Co NPs, and (002) lattice plane of graphite carbon in both the multi-walled CNT (MWCNT) and carbon shell, respectively [24]. The diffraction rings in selected area electron diffraction (SAED) (Fig. 1e) were derived from the (002) plane of carbon, as well as the (111) and (220) planes of Co NPs. The high-angle annular dark-field scanning transmission electron microscopy (HAADF-STEM), X-ray energy-dispersive spectroscopy (EDS), and elemental mapping of ZIF-8@67-C (Figs. 1f and S5) demonstrated the hollow structure of the nitrogen-doped carbon polyhedron with surface-anchored CNTs and encapsulated Co NPs. More importantly, high-density single Co atoms were clearly observed by the aberration-corrected (AC) HAADF-STEM measurement on both the carbon shell adjacent to Co NPs and the MWCNT, which were identified



Scheme 1. Schematic illustration for the synthesis procedure of the hollow graphitized carbon polyhedron with surface-anchored carbon nanotubes and supported single Co atoms (ZIF-8@67-C).

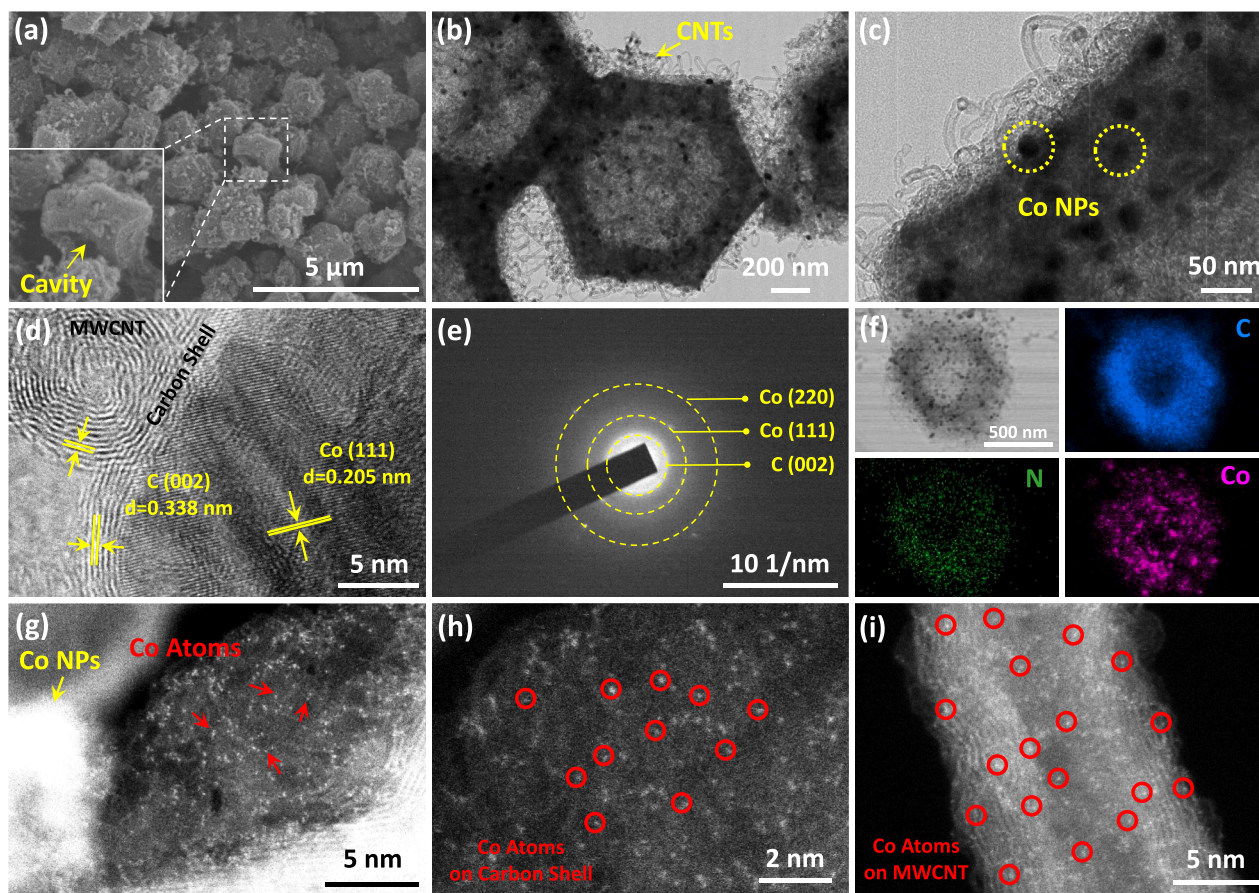


Fig. 1. (a) SEM, (b, c) TEM, (d) HRTEM, (e) SAED, (f) HAADF-STEM and EDS elemental mapping, (g–i) AC-HAADF-STEM micrographs of ZIF-8@67-C.

by isolated bright dots marked with red cycles (Figs. 1g–i).

To explore the formation mechanism of the hollow structure with surface-anchored CNTs of ZIF-8@67-C, the ZIF-8-C, ZIF-67-C and ZIF-67@8-C samples were manufactured for comparison. According to the TEM images in Figs. 1b and 2a, the hollow structure was merely

observed in ZIF-8@67-C, while only ZIF-8@67-C and ZIF-67@8-C composites possessed CNTs on the surface. Meanwhile, the X-ray diffraction (XRD, Fig. 2b) patterns of all samples other than ZIF-8-C showed peaks at 44.2°, 51.5° and 75.9° attributed to the (111), (200) and (220) crystal planes of Co NPs (PDF #15-0806) [24]. Moreover, in

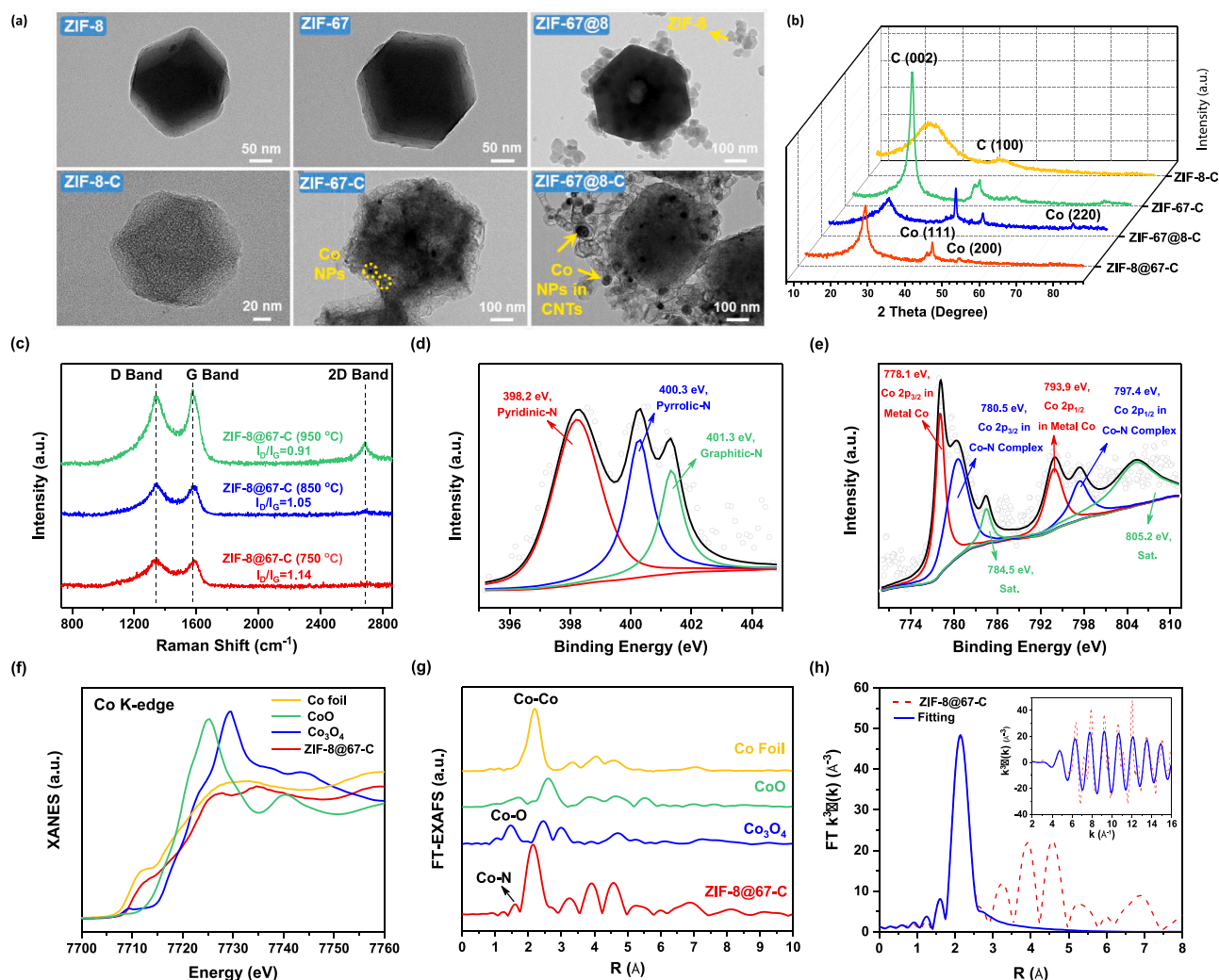


Fig. 2. (a) TEM images of ZIF-8, ZIF-67, ZIF-67@8 precursors and ZIF-8-C, ZIF-67-C, ZIF-67@8-C. The small particles around ZIF-67@8 were ZIF-8 resulting from the homogeneous assembly of Zn^{2+} and 2-methylimidazole. (b) XRD patterns of ZIF-8-C, ZIF-67-C, ZIF-67@8-C and ZIF-8@67-C. (c) Raman spectra of the ZIF-8@67-C catalysts obtained at 750, 850 and 950 °C. High-resolution XPS (d) N 1s and (e) Co 2p spectra of ZIF-8@67-C. (f) Normalized XANES spectra, (g) k^3 -weighted Fourier transform spectra of EXAFS for Co foil, CoO, Co_3O_4 and ZIF-8@67-C. (h) EXAFS fitting curves of ZIF-8@67-C.

ZIF-67-C, the intensities of peaks at 26.2° and 42.8° attributed to the (002) and (100) lattice planes of graphitized carbon were much stronger than those in ZIF-8-C (PDF #41-1487). These XRD results confirmed that Co NPs catalyzed the evolution of graphitic carbon with high crystallinity [15,25]. For ZIF-8, the organic ligands decomposed to release vast reducing gases during calcination, causing obvious volume shrinkage (Fig. 2a). Besides, the Zn^{2+} was reduced to metal Zn, which evaporated (Zn boiling point: 907 °C) to leave pure carbon without metal signals detected in the XRD pattern [26]. For ZIF-67, Co^{2+} was reduced to metal Co (Co boiling point: 2870 °C) during pyrolysis, which aggregated into Co NPs and catalyzed carbon graphitization. Because graphitic carbon possessed high thermal stability, much less gases were liberated to induce volume diminution. Actually, the sample size obviously increased due to the thermal expansion. Meanwhile, the CNTs growth was inhibited as a result of the scarce carbon-containing gas source. For ZIF-67@8, accompanying with the generation of Co NPs within the carbonized inner ZIF-67, the reducing gases from decomposed ligands in outer ZIF-8 were catalyzed by Co NPs on ZIF-67 surface to produce CNTs outwards [23]. Due to the capillary effect, some Co NPs were pumped into the nanotubes and moved along with the growing CNTs, during which the outer ZIF-8 provided abundant carbon sources to develop

thick CNTs (Fig. 2a). For ZIF-8@67, the graphite carbon shell formed by outer ZIF-67 functioned as a physical barrier to prevent the penetration of reducing gas from inner ZIF-8. These gases were then continuously deposited within the shell while only a small amount of gases could migrate to the surface and be catalyzed by Co NPs to manufacture the thin CNTs. This process proceeded until the inner ZIF-8 faded away to form the hollow structure. As Co was inevitably atomized at high temperatures, vast Co atoms diffused in the nitrogen-carbon matrix to establish atomically dispersed Co-N-C sites [27]. Moreover, even when the pyrolysis temperature for fabricating ZIF-8@67-C dropped to 850 and 750 °C, the hollow structure with surface CNTs was still present (Fig. S6). The Raman spectra in Fig. 2c exhibited obvious D, G and 2D bands at 1340, 1580 and 2687 cm^{-1} , respectively [28]. Increasing calcination temperatures from 750 to 950 °C decreased the I_D/I_G value from 1.14 to 0.91 and enhanced the 2D peak intensity, indicating that the elevated temperature favored the graphitization of carbon to generate single-to-few layer graphene-like structure [29].

The surface composition and electronic structure of ZIF-8@67-C were probed by X-ray photoelectron spectroscopy (XPS). The N 1s spectrum was deconvoluted to the peaks of pyridinic-N, pyrrolic-N and graphitic-N at 398.2, 400.3 and 401.3 eV, respectively (Fig. 2d) [30].

The peak at 398.2 eV might also include a contribution from the Co-N bond as the binding energies (BEs) of pyridinic-N and Co-N were close [31]. The Co 2p XPS spectrum was composed of the peaks assigned to the metal Co at 778.1 (2p_{3/2}) and 793.9 eV (2p_{1/2}), as well as the Co in the Co-N complex at 780.5 (2p_{3/2}) and 797.4 eV (2p_{1/2}), respectively (Fig. 2e). Two satellite peaks were also observed at 784.5 and 805.2 eV. Compared to the BEs of metal Co and oxidized Co (782.2 eV), the BE of Co 2p_{3/2} in Co-N complex exhibited an intermediate value, suggesting the Co oxidation state between 0 and +3 [23]. The X-ray absorption fine structure (XAFS) measurements were used to further detect the oxidation state and local environment of Co in ZIF-8@67-C. The normalized Co K-edge X-ray absorption near edge structure (XANES) spectra (Fig. 2f) indicated the position of the rising edge for ZIF-8@67-C was situated between those for Co foil and CoO, verifying that the average oxidation state of Co in ZIF-8@67-C was between 0 and +2 [17]. The

k^3 -weighted Fourier transform spectra of the Co K-edge extended XAFS (EXAFS) displayed distinct main peaks at 2.15 Å and higher positions, which were attributed to the Co-Co coordination shells in Co NPs of ZIF-8@67-C (Fig. 2g). Besides, the appreciable peak at 1.58 Å, corresponding to the Co-N first coordination shell, should stem from the complexes of N atoms in the carbon matrix and isolated Co atoms or Co NPs [32]. EXAFS fitting was conducted using two scattering paths of Co-Co and Co-N to obtain the quantitative Co structural configuration (Fig. 2h and Table S1). The average coordination number of the center Co atom in Co-N complexes was 2.4, indicating that one Co atom was averagely coordinated with 2.4 N atoms [32]. Considering the high atom ratio of Co/N when Co NPs reacted with neighboring N atoms in the carbon shell, the N coordination number for single Co atom possibly exceeded 2.4. The N₂ adsorption-desorption isotherm of ZIF-8@67-C exhibited a type-IV shape with the specific surface area of 467.7 m²

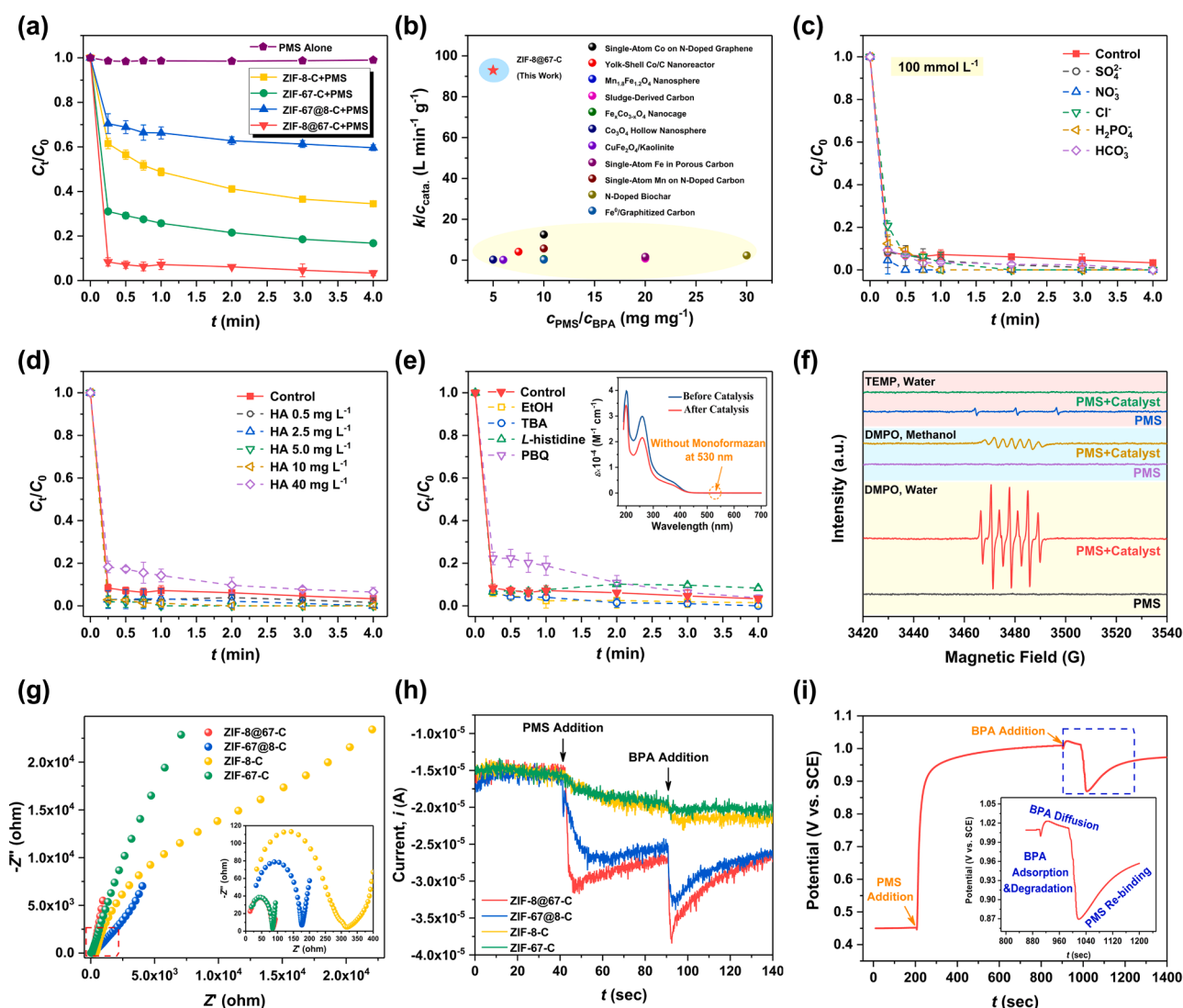


Fig. 3. (a) Kinetic curves of BPA degradation by various catalysts. (b) Comparisons of catalytic efficiency of ZIF-8@67-C with those of reported materials. (c) Influence of various inorganic anions on BPA degradation by ZIF-8@67-C. (d) Influence of different concentrations of HA on BPA degradation by ZIF-8@67-C. (e) Effect of reactive oxygen species scavengers on BPA degradation in ZIF-8@67-C/PMS system. Inset: UV-vis spectra of the NBT solutions before and after reactions. (f) EPR spectra of PMS activation by ZIF-8@67-C under various conditions with DMPO or TEMP as trappers. (g) Nyquist plots, and (h) Chronoamperometry curves with adding PMS and BPA solutions of the ZIF-8-C, ZIF-67-C, ZIF-67@8-C and ZIF-8@67-C electrodes. (i) Chronopotentiometry curve of the ZIF-8@67-C electrode with adding PMS and BPA solutions. For (h, i), added PMS: 0.5 mL, 20 g L⁻¹; added BPA: 0.5 mL, 100 mg L⁻¹. Reaction conditions for (a–f): [Catalysts] = 0.1 g L⁻¹; [PMS] = 0.1 g L⁻¹; [BPA] = 20 mg L⁻¹, pH₀ = 6.7 (for the control), T = 25 °C; [Anions] = 100 mmol L⁻¹, [EtOH] and [TBA] = 0.2 mol L⁻¹, [L-histidine] and [PBQ] = 0.02 mol L⁻¹, [DMPO] = 0.1 mol L⁻¹, [TEMP] = 0.02 mol L⁻¹ (if needed).

g^{-1} (Fig. S7 and Table S2). The H3 hysteresis loop and high uptake at low relative pressure indicated the coexistence of micropore and mesopore, matching well with the pore distribution at 1.69 and 4.88 nm, which was beneficial for the mass transport [31].

3.2. Catalytic performance and pathway

The BPA was used as a model pollutant to assess the catalytic performance. Fig. 3a showed that < 2% of BPA was degraded by PMS, suggesting the low oxidative ability of PMS alone. Contrarily, BPA concentration quickly declined after adding catalysts and the removal efficiency followed the order of ZIF-8@67-C > ZIF-67-C > ZIF-8-C > ZIF-67@8-C. Especially for ZIF-8@67-C, the residual BPA concentration ratio was reduced to 8.38% within only 15 s. The first-order kinetic equation well fitted the degradation data ($R^2 = 0.97$), and the catalyst-dose-normalized rate constant (k) of ZIF-8@67-C reached $92.92 \text{ L min}^{-1} \text{ g}^{-1}$, which exceeded those of reported materials by 1–2 orders of magnitude at similar PMS/BPA concentration ratios (Fig. 3b and Table S3) [6,17,33–41]. Moreover, increasing the pyrolysis temperature for preparing ZIF-8@67-C from 750 to 950 °C promoted the catalysis, as the higher degree of carbon graphitization and larger specific surface area at raised temperatures could enhance the conductivity of the carbon network and BPA adsorption through π - π interaction (Figs. S8–9 and Table S4). Meanwhile, although solution pH quickly decreased to ~ 3.2 during catalysis, no Co^{2+} was detected in bulk solution after reaction (Fig. S10), which validated the well encapsulation of Co NPs in carbon shells and stable N coordination for single Co atoms.

To investigate the anti-interference ability of ZIF-8@67-C, the impact of inorganic anions and humic acid (HA, a typical NOM) on BPA degradation was studied. As shown in Fig. S11, the high catalytic efficiency was well maintained after adding various anions including SO_4^{2-} , NO_3^- , Cl^- , H_2PO_4^- and HCO_3^- with the concentration of 1 or 10 mmol L^{-1} . Then, the anion concentration was further increased up to 100 mmol L^{-1} , no significant suppression of the catalysis was also observed (Fig. 3c). Inversely, due to the salting-out effect, the hydrophilic ions robbed water molecules around BPA to facilitate BPA adsorption onto hydrophobic carbon support (Fig. S12) [42], which elevated the removal ratios of BPA through enriching the pollutant [8, 43]. In HA-containing solution, except for 40 mg L^{-1} of HA slightly retarding the catalysis, the introduction of lower concentrations of HA (0.5–10 mg L^{-1}) even accelerated the reaction (Fig. 3d). The equilibrium adsorption capacity of BPA (Q_e) was recorded in Fig. S13, and the Q_e values were not obviously reduced with adding 0.5–10 mg L^{-1} of HA. Because the BPA molecule contained two benzene rings, it could be adsorbed by the hydrophobic graphitized carbon support of ZIF-8@67-C through hydrophobic and π - π interactions. Therefore, the hydrophilic HA used in the experiment could not effectively compete with BPA to be adsorbed by ZIF-8@67-C at low concentrations. Meanwhile, adding HA reduced solution pH from 6.7 to ~ 5.5 , which increased the amount of positive charges on the catalyst ($\text{pH}_{\text{PZC}} = 9.1$, Fig. S14), benefiting the electrostatic binding of PMS (HSO_5^-) to induce the higher degradation rates. As in ROSs-dominated AOP, the removal of targeted pollutants would be inhibited by anions and HA due to the ROSs consumption [6, 40], the above results implied that ROSs might not be generated.

To determine whether ROSs were involved in the ZIF-8@67-C/PMS system, the quenching tests were performed. The ethanol (EtOH) with α -H could quench both $\bullet\text{OH}$ and $\text{SO}_4^{\bullet-}$ while the *tert*-butyl alcohol (TBA) without α -H was merely effective for $\bullet\text{OH}$ but not for $\text{SO}_4^{\bullet-}$ [33]. *L*-histidine and *p*-benzoquinone (PBQ) possessed excellent reactivity with singlet oxygen ($^1\text{O}_2$) and $\text{O}_2^{\bullet-}$, respectively [10,44]. As Fig. 3e, the addition of EtOH, TBA and *L*-histidine exerted negligible influences on BPA removal, which convincingly ruled out the participation of $\text{SO}_4^{\bullet-}$,

$\bullet\text{OH}$ and $^1\text{O}_2$ in degrading BPA. Adding PBQ slightly depressed the catalysis, indicating the possible existence of $\text{O}_2^{\bullet-}$. The nitro blue tetrazolium chloride monohydrate (NBT) was further used to probe $\text{O}_2^{\bullet-}$ as it could react with $\text{O}_2^{\bullet-}$ to generate the monoformazan with the maximal absorbance at 530 nm [45]. However, the peak of monoformazan did not appear in the UV-vis spectrum after reaction, excluding the existence of $\text{O}_2^{\bullet-}$ (Fig. 3e, Inset). The declined catalytic efficiency was possibly because the hydrophobic PBQ could be adsorbed by ZIF-8@67-C and competitively consumed PMS. To further reveal the reaction process, the electron paramagnetic resonance (EPR) detections were performed in Fig. 3f. In the water phase with DMPO as the ROSs trapper, PMS alone did not release any signals, in line with the above negligible BPA removal. However, the typical seven peaks with the intensity of 1:2:1:2:1:2:1 from the DMPOX appeared with adding ZIF-8@67-C. DMPOX (5, 5-dimethyl-2-pyrrolidone-N-oxyl) was the product of DMPO reacting with a great deal of oxidants suddenly produced, which demonstrated the excellent ability of ZIF-8@67-C in PMS activation [46]. Changing the water phase to methanol phase was used to detect $\text{O}_2^{\bullet-}$ [47]. However, in the presence of ZIF-8@67-C, the peaks of DMPOX instead of typical peaks from $\text{O}_2^{\bullet-}$ were observable. The much weakened signal intensity compared to that in water phase was attributed to the depressed DMPO adsorption onto the catalyst by methanol. TEMP was used to probe $^1\text{O}_2$ because it could react with $^1\text{O}_2$ to generate a stable adduct called TEMPN (2,2,6,6-tetramethylpiperidine-N-oxyl) [10]. For PMS alone, the characteristic three-line peak from TEMPN certified the slow generation of $^1\text{O}_2$ due to the PMS self-decomposition [44]. However, the signal of $^1\text{O}_2$ became silent after adding ZIF-8@67-C, testifying that the evolution route of $^1\text{O}_2$ was hindered and replaced by another pathway. These results suggested that there was a reaction way independent of ROSs that led to rapid BPA degradation.

Yun et al. reported that the organic contaminant oxidation in CNTs/PMS system followed an electron-transfer mechanism, which preferentially occurred when the catalyst had high conductivity and high adsorbability for pollutants [10]. To gain insight into this possible route for BPA removal, the electrochemical impedance was measured and the obtained Nyquist plots were shown in Fig. 3g to evaluate the conductivity of catalysts. The semicircle and linear portions were severally assigned to the charge-transfer and mass-transfer resistances [43]. The smallest semicircle radius of ZIF-8@67-C indicated the highest conductivity to transport electrons, which accelerated the redox kinetics. Meanwhile, the fitting result of BPA adsorption isotherm by Langmuir model suggested that the maximal BPA adsorption capacity of ZIF-8@67-C reached 139.62 mg g^{-1} ($R^2 = 0.99$), surpassing those of many reported adsorbents (Fig. S15 and Table S5) [48–53]. These laid good foundations for the occurrence of the electron-transfer route. To further uncover it, the chronoamperometry curve was recorded in Fig. 3h. The addition of PMS induced a large enhancement of the current output for ZIF-8@67-C, indicating that PMS was bonded to the catalyst and exchanged electrons with the catalytic sites [43]. Adding BPA led to a further increase in the current intensity, implying the electron extraction from BPA by the catalyst. The relatively sluggish current increase and lower current intensity of ZIF-67@8-C were possibly ascribed to the higher charge-transfer resistance. Meanwhile, the small changes in the currents of ZIF-67-C and ZIF-8-C suggested that the ROSs route rather than the electron-transfer process controlled BPA degradation as reported [6,26]. The chronopotentiometry analysis in Fig. 3i exhibited that after adding PMS, the potential of ZIF-8@67-C-coated electrode rose sharply and then stabilized at $\sim 1.0 \text{ V}$ vs. SCE, indicating that PMS and catalytic sites formed the complexes and induced high redox potential [9]. With the introduction of BPA, the potential did not decrease immediately because BPA had not yet spread to the catalyst surface.

Once BPA reached the catalyst and was adsorbed, the electrons from BPA were extracted and flowed into the region with high redox potential, which caused the potential to drop rapidly. Afterwards, the residual PMS in bulk solution re-occupied the catalytic sites and formed new complexes, making the potential rise again.

3.3. Determination of catalytic site and mechanism

Identification of the active center for PMS activation was critical to understand the above electron-transfer process. As shown in Fig. S16, increasing the Co ($\text{Co}(\text{NO}_3)_2 \cdot 6\text{H}_2\text{O}$) amount for preparing ZIF-8@67 precursors from 0.05 to 0.15 mol elevated the Co weight ratios in the obtained ZIF-8@67-C from 18.75% to 27.27%, which was accompanied with an accelerated BPA degradation with k rising from 5.84 to 9.68 min^{-1} , suggesting the crucial role of Co in the catalysis. However, further elevating Co amount to 0.20 mol (Co weight ratio in ZIF-8@67-C was 30.77%) resulted in a reduced k value to 4.84 min^{-1} , which testified that besides the Co-containing site for PMS activation, the N-doped carbon (with decreased content in the catalyst when increasing Co amount) for electron conduction and BPA adsorption was also essential to quicken BPA degradation. As two Co species, i.e. the carbon encapsulated Co NPs and single Co atoms, co-existed in ZIF-8@67-C, it's significant to distinguish which Co species served as the real catalytic site for PMS activation. Bao et al. found that the metal NPs coated with < 3 layers of carbon would form a 'chainmail catalyst', in which the

electrons of metal NPs could penetrate through the carbon shell to create a reactive carbon surface for promoting the catalysis. However, when the number of carbon layers exceeded 3, the metal core became inert [54]. A careful examination of the HRTEM images revealed that the Co NPs in ZIF-8@67-C were tightly wrapped by > 6 layers of carbon, predicting the absence of Co NPs in activating PMS (Fig. S17). To further testify it, a heating NH_4Cl -treatment method was utilized to etch out Co NPs from ZIF-8@67-C without destructing the single-atom Co sites [11]. As shown in Figs. S18 and S19 (Inset), the Co NPs became less and the saturation magnetization of the catalyst decreased from 28.05 to 13.29 emu g^{-1} after NH_4Cl treatment, indicating that parts of Co NPs were successfully dislodged. Surprisingly, the catalytic activity of treated ZIF-8@67-C was even strengthened (due to more available active sites per unit of mass), which clearly suggested the negligible role of encapsulated Co NPs in PMS activation. To verify the involvement of single-atom Co site, the poisoning test with SCN^- was conducted as SCN^- could block metal-N-C site via strong coordination [11]. The catalytic efficiency of ZIF-8@67-C in the presence of SCN^- was dramatically inhibited with only 7.96% of BPA being removed within 4 min (Fig. S19), indicating that the active center in ZIF-8@67-C for PMS activation was exclusively the single-atom Co site.

The DFT calculation was used to further uncover the reaction mechanism. According to the EXAFS result, the catalyst models with single-atom CoN_4 and CoN_3C_1 sites were established for PMS binding due to the N/Co atom ratio over 2.4. The optimized binding

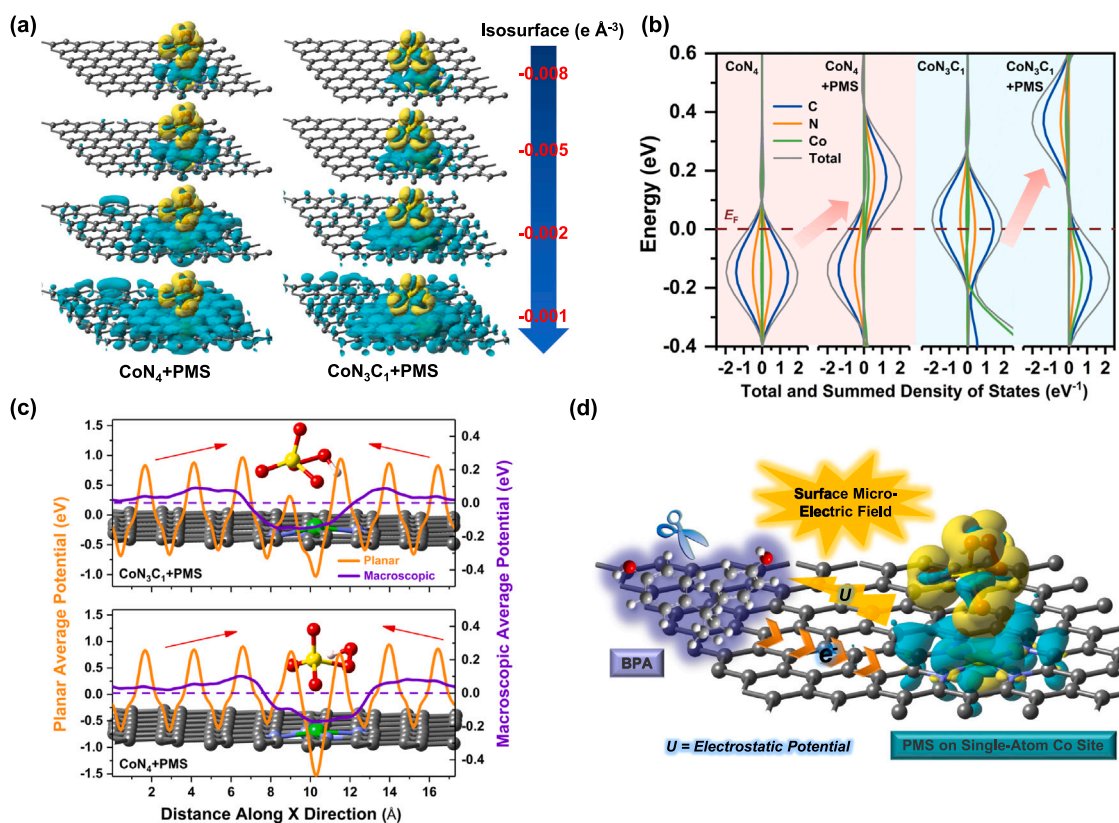


Fig. 4. (a) Charge density differences in PMS-adsorbed single-atom CoN_4 and CoN_3C_1 catalysts. The electron accumulation and depletion were denoted by the light yellow and blue green, respectively. The isosurface contour for the electron accumulation zone was $+0.01 \text{ e} \text{ \AA}^{-3}$ while the isosurface contour for the electron depletion zone ranged from -0.008 to $-0.001 \text{ e} \text{ \AA}^{-3}$. The C, O, S, N, H and Co atoms were represented by the gray, red, yellow, blue, white and green spheres, respectively. (b) Total and summed density of states (DOS) of the pristine CoN_4 catalyst, PMS-adsorbed CoN_4 catalyst (CoN_4+PMS), pristine CoN_3C_1 catalyst and PMS-adsorbed CoN_3C_1 catalyst ($\text{CoN}_3\text{C}_1+\text{PMS}$). The E_F with the energy of 0 eV represented the Fermi level. (c) Change of the planar and macroscopic average electrostatic potentials along the X direction (from left to right) of the CoN_4+PMS and $\text{CoN}_3\text{C}_1+\text{PMS}$ complexes (Insets behind the data). The macroscopic average potential was obtained by the integration of the planar average potential with the integration range of 4.92 \AA . (d) Overall catalytic reaction mechanism of BPA degradation via PMS activation on ZIF-8@67-C.

configurations of PMS on the catalyst surface were shown in Fig. S20. The adsorption energy (E_{ads}), O-O bond length and Bader charge of PMS adsorbed onto the CoN_4 center were 3.499 eV, 1.473 Å and $-0.81|e|$, while these values for the CoN_3C_1 site were 3.479 eV, 1.470 Å and $-0.73|e|$, respectively (The O-O bond length of free PMS was 1.411 Å). Therefore, the CoN_4 site was more efficient in PMS capture and activation. Noteworthy, for Co or Co-containing nanoparticles, it's well-established that low-valence Co donated one electron to one PMS, resulting in the cleavage of O-O bond to produce $\text{SO}_4^{\bullet-}$ or $\bullet\text{OH}$ (Eqs. (1)–(3)) [35]. However, for the single-atom Co sites, the PMS gained $< 1|e|$ from the catalyst, which was unable to induce O-O breakage to generate $\text{SO}_4^{\bullet-}$ or $\bullet\text{OH}$, and thus failed to fabricate $\text{O}_2^{\bullet-}$ through the chain reactions as Eqs. (4)–(6) [44]. Besides, the $^1\text{O}_2$ could not be formed as its production required PMS to lose one electron to the catalyst to generate $\text{SO}_5^{\bullet-}$ (Eqs. (7) and (8)) [55]. In a word, the low amount ($< 1|e|$) of electron acquisition by PMS restrained its conversion to ROSSs. The charge density difference analysis (Fig. 4a) visually exhibited that the electron flowed from the catalyst to PMS resulting from the electron-withdrawing effect of PMS. Meanwhile, when the isosurface contour increased from -0.008 to -0.001 e Å^{-3} , the area of electron depletion zone radially expanded with the CoN_4 or CoN_3C_1 site as the center, suggesting the region closer to the active site lost more electron upon PMS adsorption. The density of states (DOS) curves in Fig. 4b exhibited that after binding PMS, the pristine CoN_4 catalyst mainly lost spin-up electrons in occupied orbitals below the Fermi level. Correspondingly, new states associated with the vacant orbitals those could be occupied by spin-up electrons appeared with the energy centered at $\sim 0.18 \text{ eV}$ above the Fermi level. Similarly, after the adsorption of PMS, the CoN_3C_1 catalyst presented new states from vacant orbitals those could be occupied by spin-down electrons, but the energy center of these vacant orbitals shifted up to $\sim 0.37 \text{ eV}$, indicating that the CoN_3C_1 +PMS complex required to overcome higher energy barrier to receive electrons compared to the CoN_4 +PMS complex. Moreover, projecting DOS onto different atoms showed that the electrons extracted by PMS mainly came from the orbitals of C atoms, while the vacant orbitals above Fermi level those could accept electrons were also primarily composed of C orbitals, highlighting the role of the carbon support as the mediator for electron transfer in PMS activation and subsequent pollutant oxidation.

Considering that the uneven charge distribution on the catalyst would induce the surface potential difference, the planar and macroscopic average potentials were scanned along the X-axis of the CoN_4 +PMS and CoN_3C_1 +PMS complexes (Fig. 4c, Insets). It was found that the planar potentials overall followed a rising trend and the macroscopic potentials increased from both sides towards the middle PMS-adsorbed single-atom Co sites. This radiately decreasing potentials around the single-atom Co center would excite micro-electric field on the catalyst surface [56]. Consequently, the electron in the BPA adsorbed on the low-potential region was extracted by the electric field force, and orientationally migrated towards the high-potential region (the single-atom CoN_4 or CoN_3C_1 center) with the carbon support as the conductor to initiate the degradation (Fig. 4d). Meanwhile, the high-density single-atom Co sites enabled synchronous capture of vast PMS, which generated abundant surface micro-electric fields and then provided sufficiently strong electric field resultant force to rapidly extract electrons from surface-enriched BPA for ultrafast BPA decomposition [9]. Overall, the high-density single-atom Co sites, high adsorbability and high conductivity were integrated into the hollow structure without inaccessible bulk interior of ZIF-8@67-C, making it a '4H' reactor to establish the powerful pollutant-catalyst-PMS electron transfer pathway. This process did not produce any ROSSs, contributing to the excellent efficiency and anti-interference performance of the catalyst even in the presence of inorganic anions or NOM.



3.4. Influence of reaction parameters and reusability

The effect of working parameters on BPA degradation was investigated. The removal rate of BPA was enhanced when reducing BPA initial concentrations (Fig. S21 and Table S6). Increasing PMS concentration and catalyst dosage also accelerated the catalysis (Figs. S22–23). Importantly, the ZIF-8@67-C/PMS system could remove BPA at a wide pH range of 3–11 and broad reaction temperatures from 5 to 35 °C (Figs. S24–25). Based on the TOC analysis, the BPA mineralization ratio was up to 58.78% in 4 min (Fig. S26). The decomposition pathway according to the detection of intermediates (Table S7) was inferred in Fig. S27. The broad-spectrum experiment suggested that methyl orange, phenol and sulfamethoxazole were also rapidly decomposed in 4 min with the removal ratios over 93% (Fig. S28). Moreover, besides PMS, peroxydisulfate could be activated by ZIF-8@67-C as well for quick BPA degradation (Fig. S29). The above results indicated that ZIF-8@67-C was a versatile catalyst that could be used in various aqueous conditions.

The reusability of the catalyst was evaluated in Fig. S30. After the 1st reaction, ZIF-8@67-C was separated by a magnet and used in the next run. The BPA degradation ratio was found to drop to 64.70% within 4 min (Fig. S30a). The XPS spectra of Co and N after reaction in Fig. S31 showed that the obvious peaks attributed to the Co-N complex were still present, suggesting the stability of the single-atom cobalt site during catalysis. According to the wide-scan XPS spectra (Fig. S30b), the total oxygen content increased from 2.51 to 8.36 at% after reaction. Meanwhile, the C 1s core-level XPS spectra revealed that the ratio of C-O rose from 13.62% to 19.81% after catalysis (Fig. S30c) [43], and negligible degradation intermediates of BPA in bulk solution were detected in the time-dependent HPLC spectra (Fig. S30d). These results indicated that the degradation intermediates were attached on the catalyst, which caused the efficiency loss by competitively consuming PMS [17]. Heat treatment was usually used to desorb surface adsorbates from catalysts [33]. After a simple calcination in Ar at 950 °C for 2 h, ZIF-8@67-C regained the catalytic activity as the fresh version in following 3 runs, demonstrating the feasibility of thermal regeneration. The AC-HAADF-STEM images of regenerated catalyst suggested that vast single Co atoms were still anchored on the carbon support (Figs. S30e–f), in line with the above undetected Co leakage into bulk solution after reaction. The strong N coordination suppressed the detachment of Co atoms and guaranteed excellent efficiency recovery.

3.5. Construction and performance of catalytic column equipment

For treating large amounts of polluted waters, the dynamic column equipment which could continuously degrade pollutants was highly desirable to increase treatment efficiency and reduce site area. To this end, a column unit was assembled as Fig. 5a to explore the applicability of ZIF-8@67-C in practical scenarios. To maintain the dispersion of catalysts, an absorbent cotton was used as the support for ZIF-8@67-C (Fig. 5b). By dropping the catalyst dispersion solution onto the cotton that was pre-loaded in the column, a black catalytic column was

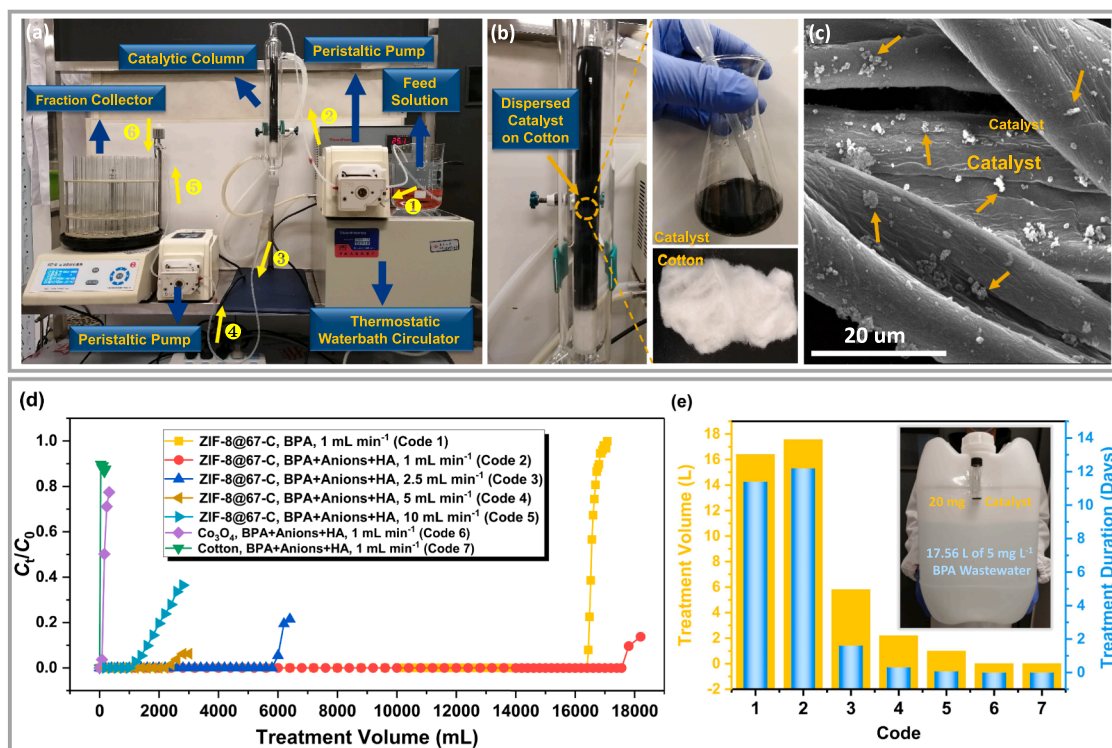


Fig. 5. (a) Photo of the catalytic column equipment. The flow direction was guided by yellow numbers and arrows. (b) Photos of the catalytic column, the catalyst dispersion solution and absorbent cotton. (c) TEM image of the ZIF-8@67-C-supported cotton fiber. (d) BPA concentration evolution in the effluent using the column equipment with commercial Co_3O_4 , pure absorbent cotton and ZIF-8@67-C in the presence/absence of anions and HA at the flow rate of 1, 2.5, 5 and 10 mL min^{-1} . The anions added to the feed solution included SO_4^{2-} , NO_3^- , Cl^- , H_2PO_4^- and HCO_3^- . Reaction conditions: Catalyst dose = 20 mg, $T = 25^\circ\text{C}$, $\text{pH}_0 = 7.5$, $[\text{BPA}] = 5 \text{ mg L}^{-1}$, $[\text{PMS}] = 0.1 \text{ g L}^{-1}$, $[\text{Anions}] = 1 \text{ mmol L}^{-1}$, $[\text{HA}] = 1 \text{ mg L}^{-1}$. (e) Total treatment volume and treatment duration of different catalysts at various conditions in (d). Inset: Photograph of the 20 mg ZIF-8@67-C powders and the BPA wastewater to be completely degraded.

obtained. The TEM image in Fig. 5c intuitively confirmed that ZIF-8@67-C was well dispersed on the cotton fiber. The BPA and PMS mixture was pumped into the column. After catalysis, the solution was collected to track the residual BPA concentration. For comparisons, commercial Co_3O_4 NPs ($\sim 30 \text{ nm}$) and pure absorbent cotton were also used to run the column tests. The results in Fig. 5d and e suggested that at a flow rate of 1 mL min^{-1} , both Co_3O_4 and cotton exhibited poor efficiencies in this system, and BPA was directly leaked in the initial 40 mL effluent. Impressively, by using ZIF-8@67-C, the reactor showed good performance to decrease the concentration of BPA from 5 to 0 mg L^{-1} for 16.40 L by loading only 20 mg of catalyst. Moreover, adding anions and HA further improved the processing efficiency and the volume of BPA that was completely degraded increased to 17.56 L, in line with the results in batch tests. In terms of treatment duration, ZIF-8@67-C enabled the system to operate steadily with no BPA leakage for as long as 12.19 days in the presence of anions and HA. When the feeding rates increased to 2.5, 5 and 10 mL min^{-1} , the total treatment volume of BPA was declined to 5.8, 2.2 and 1.0 L due to shortened hydraulic retention time, still outperforming that of commercial Co_3O_4 at 1 mL min^{-1} . This outstanding performance of ZIF-8@67-C in continuously treating wastewaters was originated from the well support/dispersion of catalysts on the cotton which prevented the catalyst loss and guaranteed high contact efficiency. Besides, the ZIF-8@67-C with both adsorption and catalytic sites could rapidly intercept BPA from flowing waters and bind PMS to excite surface micro-electric fields for ultrafast BPA degradation.

4. Conclusions

This work converted the core-shell ZIF-8@67 into a graphitized carbon polyhedral catalyst, which integrated hollow structure, high-

density single-atom Co sites, high adsorbability and high conductivity. The '4H' composite served as an efficient PMS activator for the catalytic degradation of BPA, and the catalyst-dose-normalized kinetic rate constant exceeded those of reported heterogeneous catalysts by 1–2 orders of magnitude. Moreover, the catalytic system exhibited strong anti-interference ability against inorganic anions and NOM, and could work well in wide pH and temperature ranges. Quenching tests, EPR detections and electrochemical analyses revealed the dominance of the electron-transfer mechanism responsible for BPA decomposition. DFT simulation suggested that the atomically dispersed Co sites effectively bound PMS to stimulate radial micro-electric fields on the carbon support for extracting electrons from co-adsorbed BPA. Moreover, the exhausted catalyst could be well regenerated by heat treatment. The self-constructed catalytic column equipment displayed impressive performance by realizing the continuous zero discharge of BPA for 12.19 days with loading only 20 mg of catalyst. Overall, this work could not only guide the catalyst design with '4H' characteristics for pollution control in complex water matrices, but also provide valuable atomic-level insight into the electron-transfer pathway in PMS-AOP.

CRediT authorship contribution statement

Changqing Zhu: Conceptualization, Methodology, Software, Writing – original draft, Funding acquisition. **Yu Nie:** Data curation, Investigation. **Shafei Zhao:** Visualization, Software. **Zhongwei Fan:** Data curation, Investigation. **Fuqiang Liu:** Supervision, Validation, Writing – review & editing, Funding acquisition. **Aimin Li:** Supervision, Project administration.

Declaration of Competing Interest

The authors declare that they have no known competing financial interests or personal relationships that could have appeared to influence the work reported in this paper.

Acknowledgments

This work was supported by the National Natural Science Foundation of China (51908273 and 51522805).

Appendix A. Supporting information

Supplementary data associated with this article can be found in the online version at [doi:10.1016/j.apcatb.2021.121057](https://doi.org/10.1016/j.apcatb.2021.121057).

References

- [1] A. Misra, C. Zambrzycki, G. Klokner, A. Kotyba, M.H. Anjass, I. Franco Castillo, S. G. Mitchell, R. Güttel, C. Streb, Water purification and microplastics removal using magnetic polyoxometalate-supported ionic liquid phases (magPOM-SILPs), *Angew. Chem.* 59 (2019) 1601–1605.
- [2] B.C. Hodges, E.L. Cates, J.H. Kim, Challenges and prospects of advanced oxidation water treatment processes using catalytic nanomaterials, *Nat. Nanotechnol.* 13 (2018) 642–650.
- [3] Z.Y. Guo, C.X. Li, M. Gao, X. Han, Y.J. Zhang, W.J. Zhang, W.W. Li, Mn-O covalency governs the intrinsic activity of Co-Mn spinel oxides for boosted peroxymonosulfate activation, *Angew. Chem.* 60 (2021) 274–280.
- [4] Z. Wu, Y. Wang, Z. Xiong, Z. Ao, S. Pu, G. Yao, B. Lai, Core-shell magnetic Fe₃O₄@Zn/Co-ZIFs to activate peroxymonosulfate for highly efficient degradation of carbamazepine, *Appl. Catal. B: Environ.* 277 (2020), 119136.
- [5] H. Wu, X. Xu, L. Shi, Y. Yin, L.C. Zhang, Z. Wu, X. Duan, S. Wang, H. Sun, Manganese oxide integrated catalytic ceramic membrane for degradation of organic pollutants using sulfate radicals, *Water Res.* 167 (2019), 115110.
- [6] M. Zhang, C. Xiao, X. Yan, S. Chen, C. Wang, R. Luo, J. Qi, X. Sun, L. Wang, J. Li, Efficient removal of organic pollutants by metal-organic framework derived Co/C yolk-shell nanoreactors: Size-exclusion and confinement effect, *Environ. Sci. Technol.* 54 (2020) 10289–10300.
- [7] P. Duan, Y. Qi, S. Peng, X. Peng, W. Wang, Y. Yue, Y. Shang, Y. Li, B. Gao, X. Xu, Enhanced degradation of clothianidin in peroxymonosulfate/catalyst system via core-shell FeMn @ N-C and phosphate surrounding, *Appl. Catal. B: Environ.* 267 (2020), 118717.
- [8] X. Wang, Y. Qin, L. Zhu, H. Tang, Nitrogen-doped reduced graphene oxide as a bifunctional material for removing bisphenols: Synergistic effect between adsorption and catalysis, *Environ. Sci. Technol.* 49 (2015) 6855–6864.
- [9] W. Ren, G. Nie, P. Zhou, H. Zhang, X. Duan, S. Wang, The intrinsic nature of persulfate activation and N-doping in carbocatalysis, *Environ. Sci. Technol.* 54 (2020) 6438–6447.
- [10] E.T. Yun, J.H. Lee, J. Kim, H.D. Park, J. Lee, Identifying the nonradical mechanism in the peroxymonosulfate activation process: Singlet oxygenation versus mediated electron transfer, *Environ. Sci. Technol.* 52 (2018) 7032–7042.
- [11] M.X. Chen, M. Zhu, M. Zuo, S.Q. Chu, J. Zhang, Y. Wu, H.W. Liang, X. Feng, Identification of catalytic sites for oxygen reduction in metal/nitrogen-doped carbons with encapsulated metal nanoparticles, *Angew. Chem.* 59 (2019) 1627–1633.
- [12] Y. Shang, X. Xu, B. Gao, S. Wang, X. Duan, Single-atom catalysis in advanced oxidation processes for environmental remediation, *Chem. Soc. Rev.* 50 (2021) 5281–5322.
- [13] L. Peng, X. Duan, Y. Shang, B. Gao, X. Xu, Engineered carbon supported single iron atom sites and iron clusters from Fe-rich Enteromorpha for Fenton-like reactions via nonradical pathways, *Appl. Catal. B: Environ.* 287 (2021), 119963.
- [14] H. Song, R. Du, Y. Wang, D. Zu, R. Zhou, Y. Cai, F. Wang, Z. Li, Y. Shen, C. Li, Anchoring single atom cobalt on two-dimensional MXene for activation of peroxymonosulfate, *Appl. Catal. B: Environ.* 286 (2021), 119898.
- [15] M. Xiao, Z. Xing, Z. Jin, C. Liu, J. Ge, J. Zhu, Y. Wang, X. Zhao, Z. Chen, Preferentially engineering FeN₄ edge sites onto graphitic nanosheets for highly active and durable oxygen electrocatalysis in rechargeable Zn-Air batteries, *Adv. Mater.* 32 (2020), e2004900.
- [16] X. Wang, Q. Dong, H. Qiao, Z. Huang, M.T. Saray, G. Zhong, Z. Lin, M. Cui, A. Brozena, M. Hong, Q. Xia, J. Gao, G. Chen, R. Shahbazian-Yassar, D. Wang, L. Hu, Continuous synthesis of hollow high-entropy nanoparticles for energy and catalysis applications, *Adv. Mater.* 32 (2020), 2002853.
- [17] X. Li, X. Huang, S. Xi, S. Miao, J. Ding, W. Cai, S. Liu, X. Yang, H. Yang, J. Gao, J. Wang, Y. Huang, T. Zhang, B. Liu, Single cobalt atoms anchored on porous N-doped graphene with dual reaction sites for efficient Fenton-like catalysis, *J. Am. Chem. Soc.* 140 (2018) 12469–12475.
- [18] X. Liang, D. Wang, Z. Zhao, T. Li, Z. Chen, Y. Gao, C. Hu, Engineering the low-coordinated single cobalt atom to boost persulfate activation for enhanced organic pollutant oxidation, *Appl. Catal. B: Environ.* 303 (2022), 120877.
- [19] Y. Qi, J. Li, Y. Zhang, Q. Cao, Y. Si, Z. Wu, M. Akram, X. Xu, Novel lignin-based single atom catalysts as peroxymonosulfate activator for pollutants degradation: Role of single cobalt and electron transfer pathway, *Appl. Catal. B: Environ.* 286 (2021), 119910.
- [20] P. Duan, J. Pan, W. Du, Q. Yue, B. Gao, X. Xu, Activation of peroxymonosulfate via mediated electron transfer mechanism on single-atom Fe catalyst for effective organic pollutants removal, *Appl. Catal. B: Environ.* 299 (2021), 120714.
- [21] G. Wang, C.T. He, R. Huang, J. Mao, D. Wang, Y. Li, Photoinduction of Cu single atoms decorated on UiO-66-NH₂ for enhanced photocatalytic reduction of CO₂ to liquid fuels, *J. Am. Chem. Soc.* 142 (2020) 19339–19345.
- [22] K. Czarny, B. Krawczyk, D. Szczukocki, Toxic effects of bisphenol A and its analogues on cyanobacteria *Anabaena variabilis* and *Microcystis aeruginosa*, *Chemosphere* 263 (2021), 128299.
- [23] Y. Pan, K. Sun, S. Liu, X. Cao, K. Wu, W.C. Cheong, Z. Chen, Y. Wang, Y. Li, Y. Liu, D. Wang, Q. Peng, C. Chen, Y. Li, Core-shell ZIF-8@ZIF-67-derived CoP nanoparticle-embedded N-doped carbon nanotube hollow polyhedron for efficient overall water splitting, *J. Am. Chem. Soc.* 140 (2018) 2610–2618.
- [24] Y. Gao, C. Yang, M. Zhou, C. He, S. Cao, Y. Long, S. Li, Y. Lin, P. Zhu, C. Cheng, Transition metal and metal-N_x codoped MOF-derived Fenton-like catalysts: A comparative study on single atoms and nanoparticles, *Small* 16 (2020), e2005060.
- [25] Y. Xue, Y. Li, G. Luo, K. Shi, E. Liu, J. Zhou, Using a dynamic inhibition concept to achieve content-controllable synthesis of N-coordinated Cu atoms as reversible active site toward super Li-ion capacitors, *Adv. Energy Mater.* 10 (2020), 2002644.
- [26] G. Wang, S. Chen, X. Quan, H. Yu, Y. Zhang, Enhanced activation of peroxymonosulfate by nitrogen doped porous carbon for effective removal of organic pollutants, *Carbon* 115 (2017) 730–739.
- [27] P. Yin, T. Yao, Y. Wu, L. Zheng, Y. Lin, W. Liu, H. Ju, J. Zhu, X. Hong, Z. Deng, G. Zhou, S. Wei, Y. Li, Single cobalt atoms with precise N-coordination as superior oxygen reduction reaction catalysts, *Angew. Chem.* 55 (2016) 10800–10805.
- [28] J. Wang, B. Chen, B. Xing, Wrinkles and folds of activated graphene nanosheets as fast and efficient adsorptive sites for hydrophobic organic contaminants, *Environ. Sci. Technol.* 50 (2016) 3798–3808.
- [29] Y. Lin, P. Liu, E. Velasco, G. Yao, Z. Tian, L. Zhang, L. Chen, Fabricating single-atom catalysts from chelating metal in open frameworks, *Adv. Mater.* 31 (2019), e1808193.
- [30] Z. Yang, B. Chen, W. Chen, Y. Qu, F. Zhou, C. Zhao, Q. Xu, Q. Zhang, X. Duan, Y. Wu, Directly transforming copper (I) oxide bulk into isolated single-atom copper sites catalyst through gas-transport approach, *Nat. Commun.* 10 (2019) 3734.
- [31] R. Zhao, Z. Liang, S. Gao, C. Yang, B. Zhu, J. Zhao, C. Qu, R. Zou, Q. Xu, Puffing up energetic metal-organic frameworks to large carbon networks with hierarchical porosity and atomically dispersed metal sites, *Angew. Chem.* 58 (2019) 1975–1979.
- [32] A. Han, W. Chen, S. Zhang, M. Zhang, Y. Han, J. Zhang, S. Ji, L. Zheng, Y. Wang, L. Gu, C. Chen, Q. Peng, D. Wang, Y. Li, A polymer encapsulation strategy to synthesize porous nitrogen-doped carbon-nanosphere-supported metal isolated-single-atomic-site catalysts, *Adv. Mater.* 30 (2018), e1706508.
- [33] G.X. Huang, C.Y. Wang, C.W. Yang, P.C. Guo, H.Q. Yu, Degradation of bisphenol A by peroxymonosulfate catalytically activated with Mn_{1.8}Fe_{1.2}O₄ nanospheres: Synergism between Mn and Fe, *Environ. Sci. Technol.* 51 (2017) 12611–12618.
- [34] W. Hu, W. Tong, Y. Li, Y. Xie, Y. Chen, Z. Wen, S. Peng, X. Wang, P. Li, Y. Wang, Y. Zhang, Hydrothermal route-enabled synthesis of sludge-derived carbon with oxygen functional groups for bisphenol A degradation through activation of peroxymonosulfate, *J. Hazard. Mater.* 388 (2020), 121801.
- [35] X. Li, Z. Wang, B. Zhang, A.I. Rykov, M.A. Ahmed, J. Wang, Fe₃Co_{3-x}O₄ nanocages derived from nanoscale metal-organic frameworks for removal of bisphenol A by activation of peroxymonosulfate, *Appl. Catal. B: Environ.* 181 (2016) 788–799.
- [36] J. Hu, X. Zeng, G. Wang, B. Qian, Y. Liu, X. Hu, B. He, L. Zhang, X. Zhang, Modulating mesoporous Co₃O₄ hollow nanospheres with oxygen vacancies for highly efficient peroxymonosulfate activation, *Chem. Eng. J.* 400 (2020), 125869.
- [37] X. Dong, B. Ren, Z. Sun, C. Li, X. Zhang, M. Kong, S. Zheng, D.D. Dionysiou, Monodispersed CuFe₂O₄ nanoparticles anchored on natural kaolinite as highly efficient peroxymonosulfate catalyst for bisphenol A degradation, *Appl. Catal. B: Environ.* 253 (2019) 206–217.
- [38] Y. Li, T. Yang, S. Qiu, W. Lin, J. Yan, S. Fan, Q. Zhou, Uniform N-coordinated single-atomic iron sites dispersed in porous carbon framework to activate PMS for efficient BPA degradation via high-valent iron-oxo species, *Chem. Eng. J.* 389 (2020), 124382.
- [39] J. Yang, D. Zeng, Q. Zhang, R. Cui, M. Hassan, L. Dong, J. Li, Y. He, Single Mn atom anchored on N-doped porous carbon as highly efficient Fenton-like catalyst for the degradation of organic contaminants, *Appl. Catal. B: Environ.* 279 (2020), 119363.
- [40] L. Xu, C. Wu, P. Liu, X. Bai, X. Du, P. Jin, L. Yang, X. Jin, X. Shi, Y. Wang, Peroxymonosulfate activation by nitrogen-doped biochar from sawdust for the efficient degradation of organic pollutants, *Chem. Eng. J.* 387 (2020), 124065.
- [41] M. Li, R. Luo, C. Wang, M. Zhang, W. Zhang, P.K. Klu, Y. Yan, J. Qi, X. Sun, L. Wang, J. Li, Iron-tannic modified cotton derived Fe⁰/graphitized carbon with enhanced catalytic activity for bisphenol A degradation, *Chem. Eng. J.* 372 (2019) 774–784.
- [42] Y. Zhang, C. Zhu, F. Liu, Y. Yuan, H. Wu, A. Li, Effects of ionic strength on removal of toxic pollutants from aqueous media with multifarious adsorbents: A review, *Sci. Total Environ.* 646 (2019) 265–279.
- [43] C. Zhu, S. Zhao, Z. Fan, H. Wu, F. Liu, Z. Chen, A. Li, Confinement of CoP nanoparticles in nitrogen-doped yolk-shell porous carbon polyhedron for ultrafast catalytic oxidation, *Adv. Funct. Mater.* 30 (2020), 2003947.
- [44] Y. Zhao, H. An, J. Feng, Y. Ren, J. Ma, Impact of crystal types of AgFeO₂ nanoparticles on the peroxymonosulfate activation in the water, *Environ. Sci. Technol.* 53 (2019) 4500–4510.
- [45] C. Zhu, Y. Zhang, Z. Fan, F. Liu, A. Li, Carbonate-enhanced catalytic activity and stability of Co₃O₄ nanowires for ¹O₂-driven bisphenol A degradation via

- peroxymonosulfate activation: Critical roles of electron and proton acceptors, *J. Hazard. Mater.* 393 (2020) 122395.
- [46] Y.F. Huang, Y.H. Huang, Behavioral evidence of the dominant radicals and intermediates involved in bisphenol A degradation using an efficient Co^{2+} /PMS oxidation process, *J. Hazard. Mater.* 167 (2009) 418–426.
- [47] R. Yuan, C. Yue, J. Qiu, F. Liu, A. Li, Highly efficient sunlight-driven reduction of Cr(VI) by $\text{TiO}_2/\text{NH}_2\text{-MIL-88B(Fe)}$ heterostructures under neutral conditions, *Appl. Catal. B: Environ.* 251 (2019) 229–239.
- [48] W. He, X. Ren, Z. Yan, J. Wang, L. Lu, Porous β -cyclodextrin nanotubular assemblies enable high-efficiency removal of bisphenol micropollutants from aquatic systems, *Nano Res.* 13 (2020) 1933–1942.
- [49] K. Rekos, Z.C. Kampouraki, C. Sarafidis, V. Samanidou, E. Deliyanni, Graphene oxide based magnetic nanocomposites with polymers as effective bisphenol-A nano-adsorbents, *Materials* 12 (2019), 1987.
- [50] M.H. Dehghani, M. Ghadermazi, A. Bhatnagar, P. Sadighara, G. Jahed-Khaniki, B. Heibati, G. McKay, Adsorptive removal of endocrine disrupting bisphenol A from aqueous solution using chitosan, *J. Environ. Chem. Eng.* 4 (2016) 2647–2655.
- [51] S. Salehinia, S.M. Ghoreishi, F. Maya, V. Cerdà, Hydrophobic magnetic montmorillonite composite material for the efficient adsorption and microextraction of bisphenol A from water samples, *J. Environ. Chem. Eng.* 4 (2016) 4062–4071.
- [52] Z. Luo, H. Chen, S. Wu, C. Yang, J. Cheng, Enhanced removal of bisphenol A from aqueous solution by aluminum-based MOF/sodium alginate-chitosan composite beads, *Chemosphere* 237 (2019), 124493.
- [53] S. Liu, P. Wu, M. Chen, L. Yu, C. Kang, N. Zhu, Z. Dang, Amphoteric modified vermiculites as adsorbents for enhancing removal of organic pollutants: Bisphenol A and Tetrabromobisphenol A, *Environ. Pollut.* 228 (2017) 277–286.
- [54] J. Deng, L. Yu, D. Deng, X. Chen, F. Yang, X. Bao, Highly active reduction of oxygen on a FeCo alloy catalyst encapsulated in pod-like carbon nanotubes with fewer walls, *J. Mater. Chem. A* 1 (2013) 14868.
- [55] X. Mi, P. Wang, S. Xu, L. Su, H. Zhong, H. Wang, Y. Li, S. Zhan, Almost 100 % peroxymonosulfate conversion to singlet oxygen on single-atom CoN_{2+2} sites, *Angew. Chem.* 60 (2021) 4588–4593.
- [56] J. Chen, G. Zou, W. Deng, Z. Huang, X. Gao, C. Liu, S. Yin, H. Liu, X. Deng, Y. Tian, J. Li, C. Wang, D. Wang, H. Wu, L. Yang, H. Hou, X. Ji, Pseudo-bonding and electric-field harmony for Li-rich Mn-based oxide cathode, *Adv. Funct. Mater.* 30 (2020), 2004302.